

Sripati Sah¹

Persimmon Technologies Corp.,
Wakefield, MA 01880

Numpon Mahayotsanun¹

Department of Mechanical Engineering,
Faculty of Engineering,
Khon Kaen University,
Khon Kaen 40002, Thailand

Michael Peshkin

Department of Mechanical Engineering,
Northwestern University,
Evanston, IL 60208

Jian Cao

Department of Mechanical Engineering,
Northwestern University,
Evanston, IL 60208

Robert X. Gao

Department of Mechanical
and Aerospace Engineering,
Case Western Reserve University,
Cleveland, OH 44106

Pressure and Draw-In Maps for Stamping Process Monitoring

This paper presents two tooling-integrated sensing techniques for the in situ measurement and analyses of pressure distribution at the tool–workpiece interface and material draw-in during the stamping processes. Specifically, the contact pressure distribution is calculated from the measurements by an array of force sensors embedded in the punch, whereas sheet draw-in is measured by custom-designed thin film sensors integrated in the binder. Quantification of the pressure distribution from spatially distributed sensors has been investigated as a regularization problem and solved through energy minimization. Additionally, a Bayesian framework has been established for combining finite-element analysis (FEA) based estimates of the pressure distribution with experimentally measured evidence, to achieve improved spatiotemporal resolution. A new data visualization technique termed pressure and draw-in (PDI) map has been introduced, which combine spatiotemporal information from the two sensing techniques into an illustrative representation by capturing both the tool–workpiece interaction (dynamic information) and resulting workpiece motion (kinematic information) in a series of time-stamped snapshots. Together, the two separate yet complementary process-embedded sensing methods present an effective tool for quantifying process variations in sheet metal stamping and enable new insight into the underlying physics of the process. [DOI: 10.1115/1.4033039]

Keywords: draw-in sensing, embedded pressure sensing, stamping process monitoring, TPS surfaces, Bayesian inference

1 Introduction

Sheet metal stamping is a value-addition process that provides shape and strength to sheet metal stock. Sheet metal stamped parts have a ubiquitous presence in the automobile, aviation, naval, machine tool, and canned beverage industries. The most important reason for the broad utilization of stamped parts is the high speed associated with the process. Depending on the size and shape of the part, up to 60–100 parts can be made per minute. Second, the stamping process increases the stiffness of the sheet metal part due to cold working and out-of-plane deformations, thus strong parts can be made of relatively light weight, thin, and deformable sheet metal parts, one such example is of aluminum beverage cans made from sheet metal stock. Finally, multistage stamping operations can achieve a number of different manufacturing operations such as bending, blanking, embossing, and drawing in a single machine through one part fixture.

A basic panel stamping process is illustrated in Fig. 1. The sheet metal stock is centered on the die manually or through automatic feed systems. Proper alignment of the stock is ensured by guide pins, grooves, or similar mechanisms. During the stamping process, the periphery of the sheet metal is gripped between the die and the binder. The binder force suppresses the wrinkling tendency of the sheet metal which stems from the compressive stresses that develops in the sheet metal during the stamping process. Furthermore, the distribution of the binder force controls the amount of draw-in motion that the sheet metal edge can experience during the process. This has a direct effect on the tensile stresses in the side walls of the stamped part.

Sheet metal forming continues to be one of the topics of interest to the manufacturing community, and recent studies have investigated assumptions made in analytical modeling of failure mechanisms of forming [1]. Previous research in quality and process monitoring of stamping processes has also shown that the repeatability of the interaction between the tool and workpiece has a

strong impact on the geometric consistency of the stamped product. Variations in the tool–workpiece interaction are also reflected in the kinematics of the sheet metal motion during the process. The sheet metal motion is characterized by the draw-in parameter. Draw-in refers to the movement of the sheet metal edge between the binder and the die flange during the stamping process.

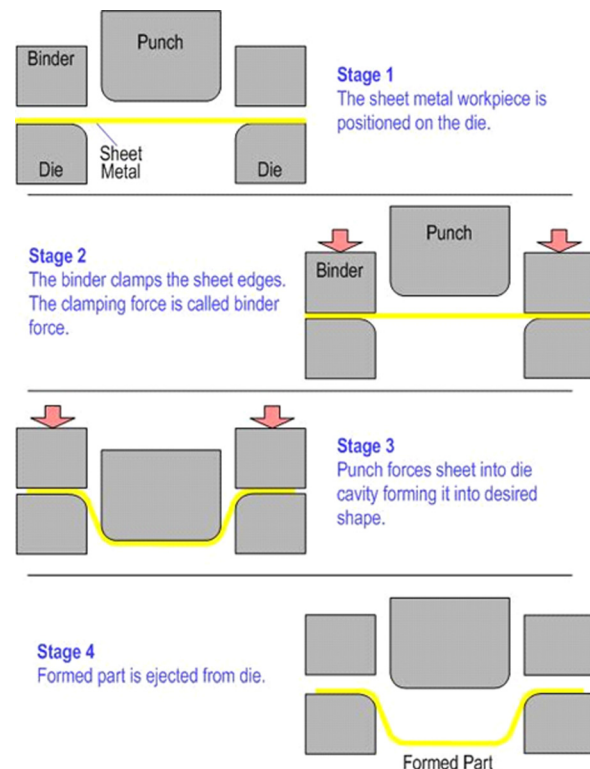


Fig. 1 Illustration of the physical setup of stamping operation

¹S. Sah and N. Mahayotsanun contributed equally to this work.

Manuscript received November 15, 2015; final manuscript received March 8, 2016; published online June 20, 2016. Assoc. Editor: Matteo Strano.

The draw-in amount is an important manufacturing index in sheet metal forming and is an indicator of the success of a forming process. Insufficient draw-in of sheet material is concomitant with the appearance of splits and excessive thinning in stamped parts while excessive draw-in leads to wrinkling and other surface defects in the stamped part.

In the area of stamping process control, various methods have been investigated to control process variables, such as blank-holder force and pressure [2]. The force control approach is shown to be augmented by forming models and referencing an optimal punch force trajectory [3]. A variant of model-based force control leverages spatially optimized blank-holder force control to improve forming limits of aluminum [4]. These studies indicate that the field of spatially optimized control can benefit from the real-time data generated by spatial-temporal sensing techniques presented in this work. Furthermore, the data measured in real-time can serve as input for online failure prediction models, such as wrinkling and tearing, as described in Refs. [5–7]. Beyond process control, the sensing techniques presented in this work can help in identifying the sources of variations in sheet metal stamping, which can augment statistical or probabilistic models for tracking variations [8–10] and establish a relationship between statistical measures of spatiotemporal sensor data and variations in part quality. The importance of spatiotemporal information in monitoring, control, and diagnosis of sheet metal stamping is increasingly realized [11]. However, the complex infrastructure required to obtain such information has presented a challenge. As technology continues to advance, various sensors, machine control systems, and process control models have been integrated to monitor process variables and observe the parts quality [12]. Beyond stamping processes, tooling embedded sensors can provide input for predictive models and help improve the accuracy and reliability of the prediction [13], by providing in situ high-quality sensing data for other manufacturing processes as well.

Online measurement of the tool-workpiece interaction and sheet metal draw-in through tooling-integrated sensors has been the subject of much research. Some of the important research works in this field are illustrated in Fig. 2. The shoulder sensor illustrated on the top right corner is designed to measure the tension in the sheet metal workpiece [14]. The sensor is installed on the die shoulder between the punch and binder and consists of a wheel which rotates with the sheet metal motion. The roller is supported by strain gauge-integrated steel webbings. During the stamping

operation, the deformation in the webbings induced by the sheet material dynamics is measured by the strain gauges. These strain measurements are used to back calculate the tension in the sheet metal. Another study investigated the use of piezoelectric sensors integrated into the binder structure to examine the effect of draw bead height on the local binder force and the sheet pulling force [15]. This study also investigated the effect of embedding depth on the response for piezosensors embedded in epoxy mediums.

In addition to embedded force sensing, prior research has also focused on finding means to measure the motion of the sheet metal during the stamping process. A sensor that measures sheet metal motion [16] is illustrated on the top left corner of Fig. 2. This design consists of a toothed friction wheel that rotates with sheet metal motion. The rotation of the wheel is sensed by a photoelectric fiber arrangement. A second type of material motion sensor illustrated on bottom left utilizes imaging algorithms similar to those used in optical mouse technology [17].

The present investigation seeks to expand on the prior work by integrating force sensors into the stamping punch (prior research has focused on sensors in binder and die shoulders) and draw-in sensors into the binder, for simultaneous measurement of stamping dynamics and kinematics in stamping processes. This concept is illustrated in Fig. 2. By integrating both force and draw-in information in a single graph called the stamping PDI map, this work provides new insights into the dynamics of the stamping process, which has been traditionally regarded as a black-box process in the industry. As a new data visualization technique, the PDI maps combine spatiotemporal information from two separate yet complementary sensing techniques into a readily understood representation, without compromising the physical significance of the data.

The remainder of this paper is organized into four sections. The first section describes the sensing principle of the tooling embedded PDI sensors as well as their design and experimental characterization. In the second section, a large-scale experimental setup with integrated PDI sensing and obtained sensor measurements is presented. The third section introduces numeric and model-based methods for pressure reconstruction from the sensor measurements. The results are presented in the fourth section, where embedded sensor measurements from the experiments are used to generate stamping PDI maps that provide a holistic picture of the stamping process. Finally, conclusions from the presented work are drawn.

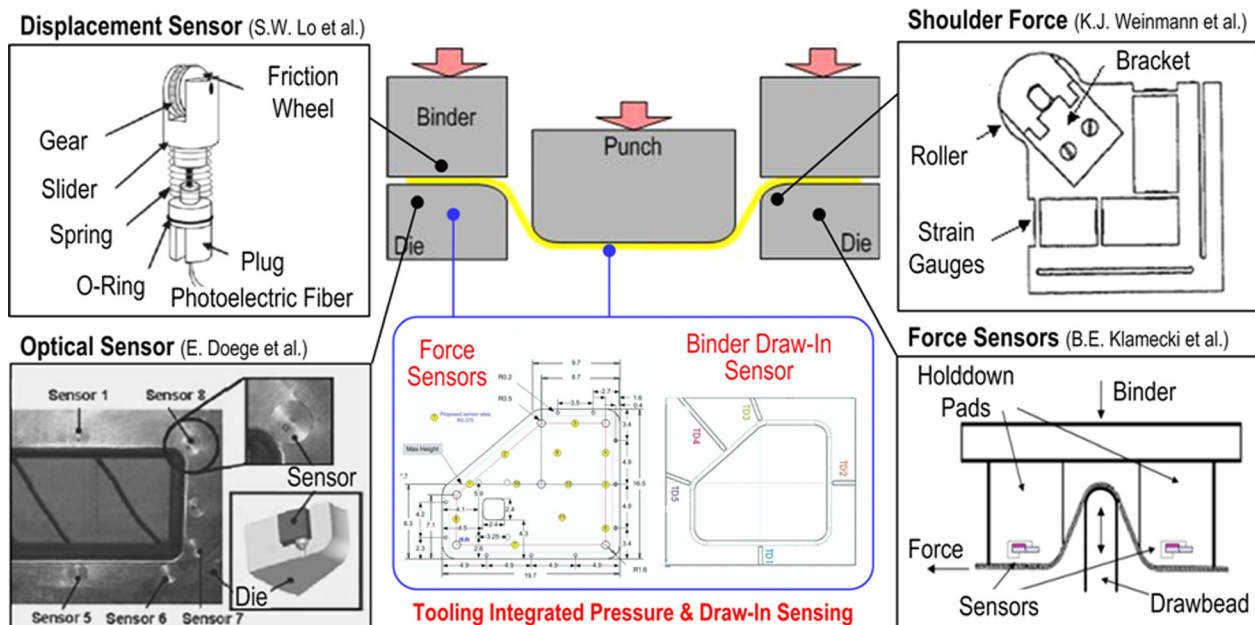


Fig. 2 Current state of sensing and the proposed technique

Table 1 Specifications of piezoquartz sensors used in the experimental study

Sensitivity	0.225 mV/N
Linearity error	$< \pm 1\%$ full scale
Footprint	$\Phi 18$ mm
Resonant frequency	7.5 kHz
Time constant	2000 s
Operational range	0–22.24 kN
Stiffness	200 N/ μ m

2 Sensing Principle

Sensors have been integrated into the punch and die flange to simultaneously measure contact pressure distribution at tool–workpiece interfaces and sheet material draw-in. The contact pressure is numerically estimated from force measurements realized by an array of piezoquartz-based sensors embedded into the punch working surface. The draw-in measurements are made by mutual inductance measurements made by opposing pairs of thin film coils embedded on the die flange and binder surfaces. This section presents a discussion on the design and characterization of the sensing principles.

2.1 Embedded Pressure Sensing. Conventional sensing methods that include pressure indicating films or ink microcapsule based systems are unable to measure the dynamics of the process while piezoresistive cells based matrix sensor mats are not robust enough to operate under the harsh manufacturing conditions present inside the stamping press [18]. To overcome these limitations, the contact pressure at the punch–sheet metal interface is measured by means of commercially available hermetically sealed piezoquartz sensors integrated on the tool surface. The operational specifications of the sensor are described in Table 1.

This sensor integration method is referred to as the top-mount technique. The schematic for a top-mount sensor is illustrated in Fig. 3 (left). The critical design parameter is the distance by which the sensor protrudes from the surface of the stamping tool, referred to as clearance. The sensor assembly consists of two components: The sensor that is threaded into a stepped through hole on the die surface and an impact cap that fits on top of the sensor. This cap is made of steel and is ground to conform with the local geometry of the tool surface. Figure 3 illustrates examples of top-mount sensors integrated into flat and convex geometries.

There is a direct effect of the embedding clearance on the behavior and response of the top-mount sensor. This effect can be better understood from the pressure distributions illustrated in Fig. 4. The top row of plots in Fig. 4 shows the contact pressure distribution around a top-mount sensor with a diameter of 18 mm embedded in the center of a contact area of diameter 77 mm. Going left to right, the net load on the contact area is the same (200 N) for all the tests but the clearance increases from a ground

finish to 50.8 μ m. In the experimental setup, the clearance is controlled by introducing precision steel shim sheets in steps of 0.0127 mm (0.0005 in.) between the sensor and the impact cap. The bottom row of plots illustrates the same information when the sensor is embedded in a cylindrical contact surface.

It is noted that as the embedding clearance increases, i.e., the sensor gets higher than the surrounding surface, the local pressure distribution tends to concentrate on the sensor surface. Such local distortions of the pressure distribution change the original in situ pressure distribution and hence need to be avoided. Thus, a low embedding clearance such as that provided by a ground finish is desirable for making pressure measurements without altering the contact pressure field that is being measured.

Further experiments were performed to investigate the role of the magnitude of the surface load and the embedding clearance on the performance of the top-mount sensor ($C = 0$ refers to ground finish). The graph in Fig. 5 indicates the response of the embedded sensor to different loads applied at the contact interface. The tests were conducted with a 0.5 mm thick Al1100 sheet metal placed between the contact surfaces. The horizontal axis in the figure represents the load applied to the contact surface, and the vertical axis denotes the force measured by the embedded sensor. Each response curve in the figure represents the response of the sensor to 27 different test load cases. The error bars indicate the maximum observed variation in five repetitions of the same load case experiment. It is noted that the sensor’s operational range is 0–22 kN; therefore, the response curves do not extend over this range.

It is further observed that in general, larger clearances lead to higher sensor response to surface loads confirming the observations made in Fig. 4. An interesting finding is that for certain embedding clearances, the sensor responds in a bilinear manner to the surface applied loads. Interestingly, the bilinear behavior is only observed for a certain range of clearance values. With zero clearance, the sensor behavior is linear, and the same is true for clearance values greater than 0.0381 mm. However for $C = 0.0381$ mm and $C = 0.0508$ mm, the slope of the response is much higher than the slope of the linear response for $C = 0$ mm. Furthermore, for $C = 0.0127$ mm and $C = 0.0254$ mm, the bilinear response is clearly present. It is also noted that for these cases, the repeatability in the lower segment (of the bilinear behavior) is much lower than that in the latter segment, as indicated by the error bars.

Further analysis indicates that the impact cap clearance imposes operational limits on the range of sensor measurements. These limits can be explained by examining two limiting values of the clearance C . For $C > 0.0381$ mm, experiments indicate that the sensor was experiencing the full applied load force. In this extreme case, the impact cap is protruding above the surrounding contact surface to such a limit that no meaningful measurements are possible. In the other extreme case where $C < 0$ mm, the impact cap is below the contact surface, and no measurement can be effectively achieved. However, this does not define the lower

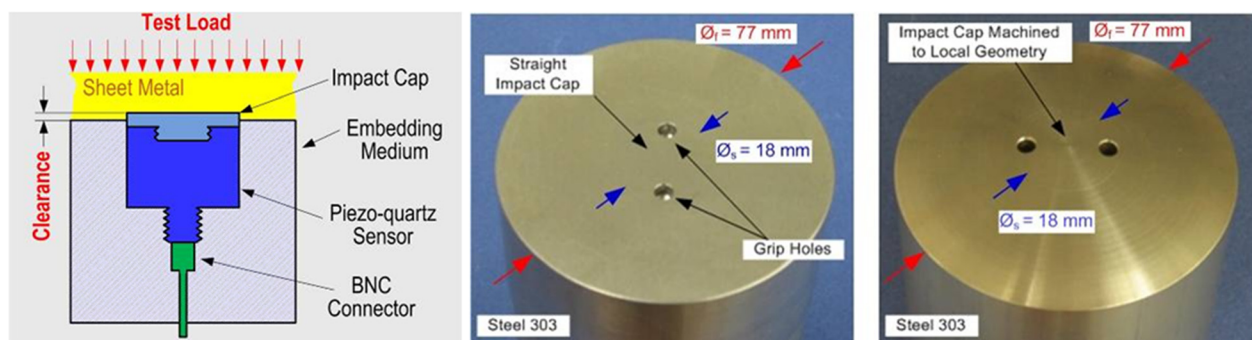


Fig. 3 Top-mount sensing schematic and prototypes

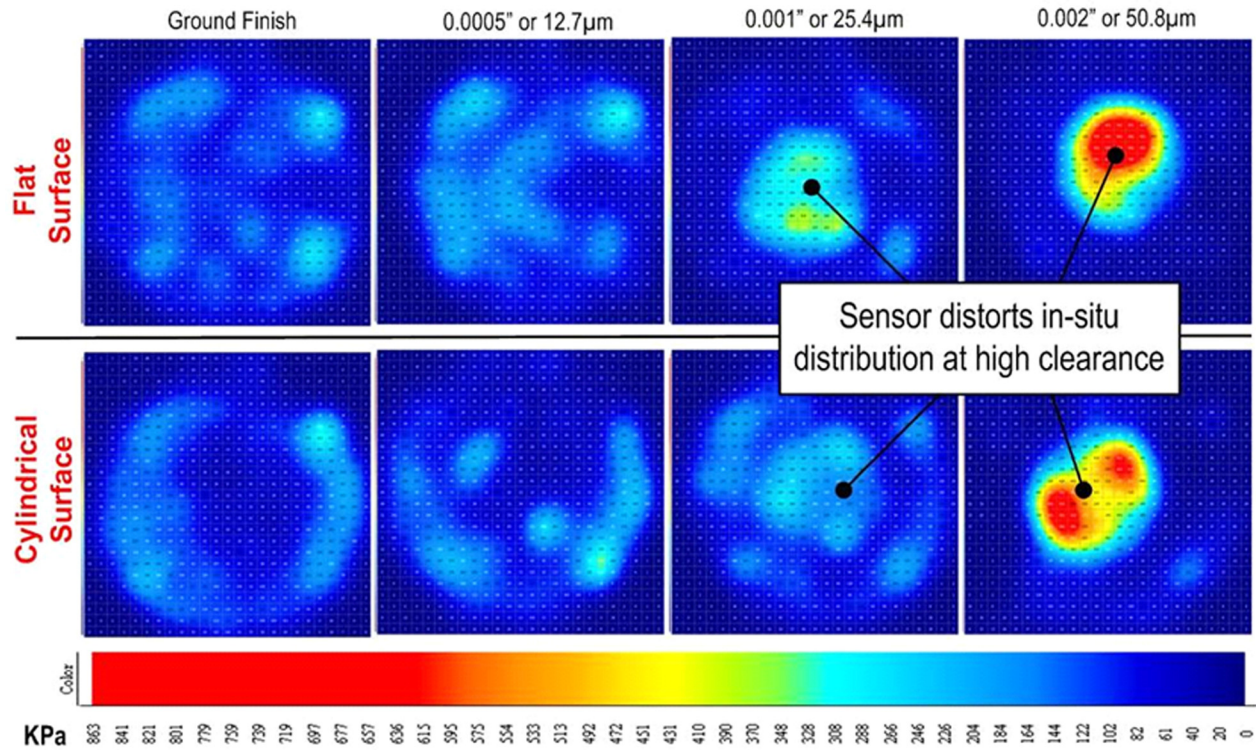


Fig. 4 Effect of embedding clearance on local pressure distribution

operational limit. The lower operational limit of the sensor measured force is the force that would act on the sensor when the impact cap is theoretically flush with the contact surface, and the pressure distribution over the entire contact surface is uniform. In this scenario, the force on the sensor could be estimated by the following expression:

$$F_{\text{Measured}}^{\text{Sensor}} = \frac{A_{\text{Sensor element}}}{A_{\text{Contact surface}}} F_{\text{Contact}}^{\text{Surface}} \quad (1)$$

Here, $A_{\text{Sensor element}}$ is the area of the sensing element, $A_{\text{Contact surface}}$ is the area of the contact surface, and $F_{\text{Contact}}^{\text{Surface}}$ is the net force acting on the contact region.

The measured force is bound by these limits and defines the operational range for the sensor. These limits are shown as

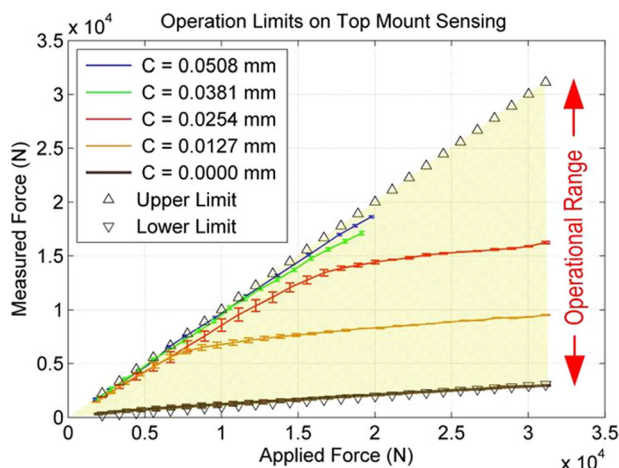


Fig. 5 Effect of clearance on top-mount sensor performance

triangles superposed over the sensor response graph. For visual clarity, the operational range has been shaded gray. It is found that for the ground clearance ($C=0$), the sensor response is almost the same as the theoretical lower limit, and for $C=0.0381$ mm and 0.0508 mm the response coincides with the upper limit. This suggests that at these clearances, the sensor is operating at the operational limits. The linear sensor response and high repeatability of the experimental measurements suggest that it is feasible to perform embedded pressure measurements with a ground finish of the sensor impact cap.

2.2 Draw-In Sensing. A draw-in sensor is developed by using the principle of mutual inductance [19–21] as seen in Fig. 6. A current is excited in the primary coil, which induces electromotive force (EMF) or induced voltages in the secondary coil as shown on the left of Fig. 6. The presence of metal (ferrous or non-ferrous) near the coils changes the degree of mutual inductance as displayed on the right of Fig. 6. Thus, the induced signal in the secondary coil (changed EMF) reflects how much of the coil is covered up.

In order to predict the sensor characteristics and to create a design guideline for the draw-in sensor, the analytical model was developed to determine the sensitivity of key design parameters, such as the gap between the two coils (D) and the coil width (W) and coil length (L), as shown in Fig. 7.

The magnetic field in the secondary coil is first calculated as the result of the current in the primary coil (Eq. (2)), followed by the calculation of the magnetic flux (Eq. (3)), and the induced EMF (Eq. (4)) in the secondary coil [22]. Note that for simplicity, this analytical model does not include the electromagnetic properties of the materials

$$B = \left(\frac{2N_1 L W \mu_0 i}{4\pi} \right) \left[\frac{1}{\left(\frac{W^2}{4} + D^2 \right)^{\frac{3}{2}}} + \frac{1}{\left(\frac{L^2}{4} + D^2 \right)^{\frac{3}{2}}} \right] \quad (2)$$

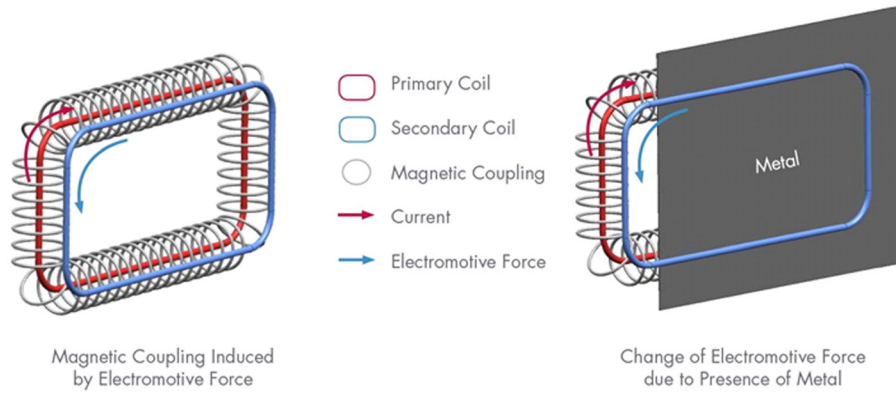


Fig. 6 Draw-in sensor based on the mutual inductance

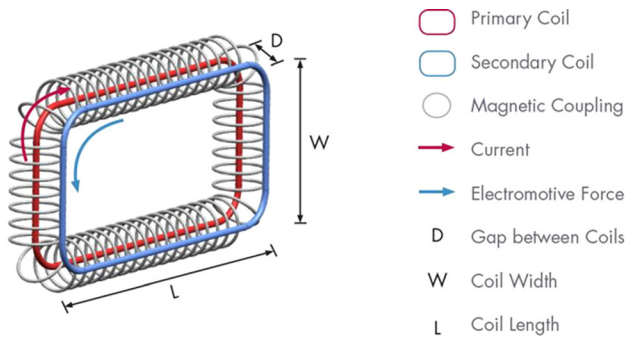


Fig. 7 Schematic of draw-in sensor for induced EMF calculation

where N_1 is the number of primary coils, L is the coil length of the uncovered zone, W is the coil width, μ_0 is the permeability constant of air ($4\pi \times 10^{-7}$ H/m), i is the excitation current (20 mA in our setup), and D is the gap distance between the two coils. Then, the magnetic flux through the secondary coil can be obtained as follows:

$$\Phi_B = \int \mathbf{B} \cdot d\mathbf{A} \quad (3)$$

where Φ_B is the magnetic flux, and \mathbf{A} is the area of the secondary coil. Finally, by using the Faraday's law, the induced EMF in the secondary coil can be computed as

$$\varepsilon = \frac{-N_1 N_2 L^2 W^2 \mu_0 i_0 f \cos(2\pi f t)}{2} \left[\frac{1}{\left(\frac{W^2}{4} + D^2\right)^{\frac{3}{2}}} + \frac{1}{\left(\frac{L^2}{4} + D^2\right)^{\frac{3}{2}}} \right] \quad (4)$$

where ε is the induced EMF, N_2 is the number of secondary coils, f is the excitation frequency (64 kHz), and t is the time.

It can be observed from Eq. (4) that the induced EMF increases with the number of primary and secondary coils, coil width, and coil length. However, the EMF decreases with the gap between the primary and secondary coils. In order to take into account the effects of electromagnetic properties of the metal covering the magnetic coupling area between the two coils, a simple simulation is developed similar to that of Fig. 6 by using the electromagnetic simulation software "INFOLYTICA-MAGNET," as illustrated in Fig. 8. The coil width and length of the primary and secondary coils are 12.7 mm and 100 mm, respectively. The gap between the two coils is 0.76 mm, which is the thickness of the metal sheet. The material of the two coils is copper, and the sheet material is AA3003. The electromagnetic simulation result is displayed in Fig. 9. When the sheet fully covers the coils, there is no induced EMF. The induced EMF increases linearly with the sheet displacement away from the coils. Various types of sheet materials and thicknesses have been simulated. The findings from all of the simulation results show that the induced EMF increases with decreasing magnetic permeability of sheet materials. Increasing sheet thickness causes the induced EMF to decrease due to the enlarging gap between the two coils.

Based on the preliminary findings from the analytical model and simulation results, a transducer of both primary and secondary coils is developed as shown in Fig. 10. The design of the

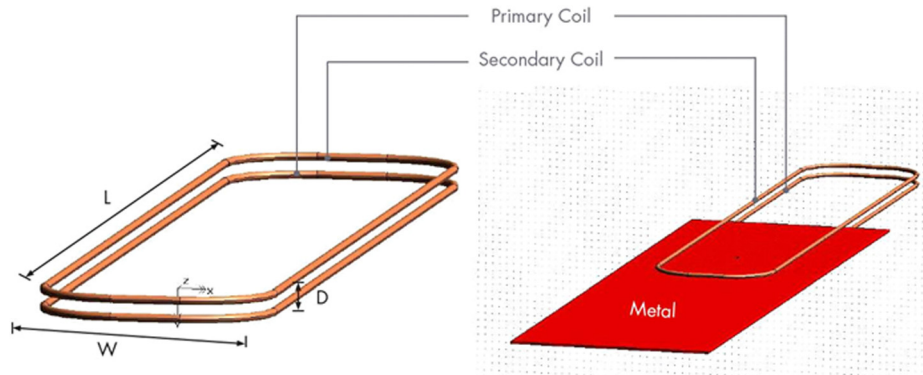


Fig. 8 Schematic of electromagnetic simulation considering the electromagnetic properties of the metal

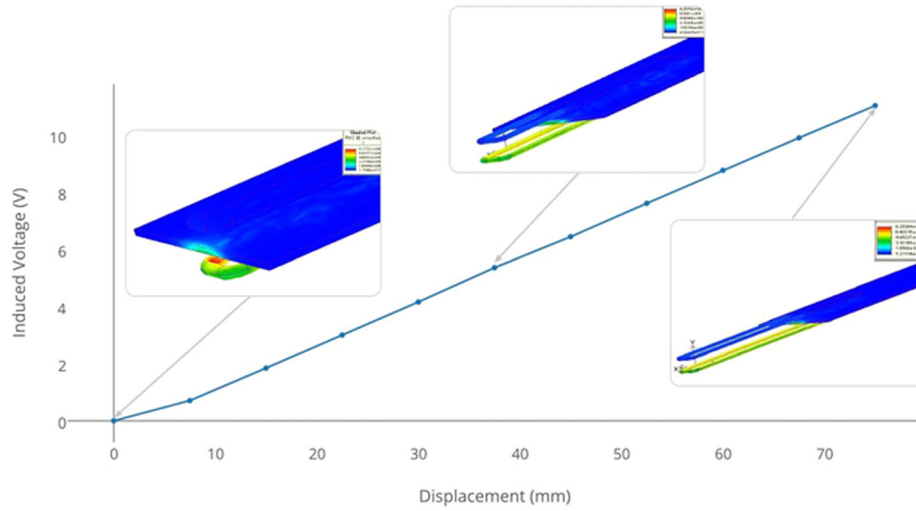


Fig. 9 Electromagnetic simulation results of induced voltage (EMF) versus displacement of AA3003 sheet having 0.76 mm thickness



Fig. 10 Draw-in sensor transducers design and development

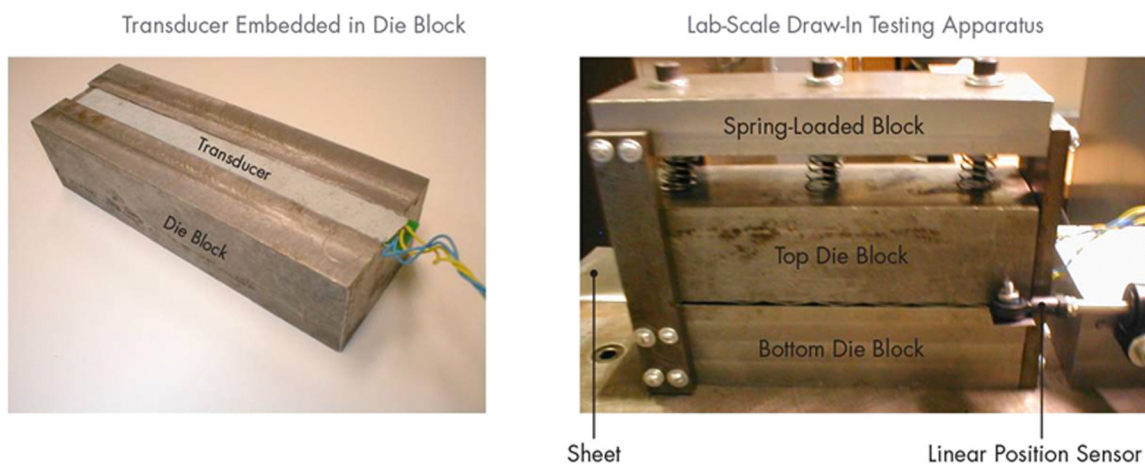


Fig. 11 Lab-scale draw-in testing apparatus

transducer is shown on the left of Fig. 10. The physical product is a silicon trace embedded in a prototype circuit board, which is shown in the center of Fig. 10. The surface of the transducer can be covered with a thin layer of epoxy (0.76 mm) to prevent scratch

from the sliding sheet metal as shown on the right of Fig. 10. The same kind of epoxy has been utilized in die repair in industry.

In order to determine the feasibility and performance of the developed transducer, a lab-scale (20 cm long) stamping simulator

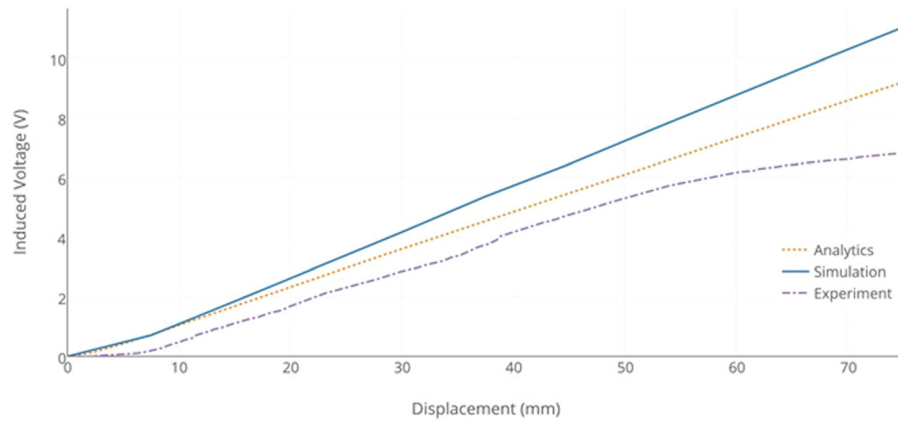


Fig. 12 Induced voltage versus displacement of AA3003 sheet having 0.76 mm thickness

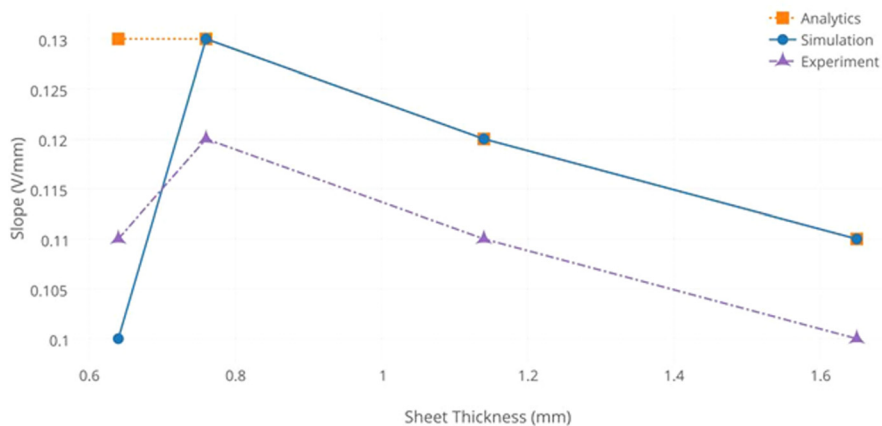


Fig. 13 Slope (induced voltage/displacement) versus sheet thickness comparison

is constructed as shown in Fig. 11. A transducer is inserted into a slot in the die block as shown on the left of Fig. 11. The primary transducer is inserted in the bottom die block, and the secondary transducer is located in the top die block as displayed on the right of Fig. 11. A sheet metal is placed in between and fully covered the two transducers at the initial stage. During the experiment, the sheet metal is pulled out of the die blocks, changing the magnetic coupling area and the induced voltages. The induced voltage signals are then recorded with the pulling distance of the sheet. To calibrate this new draw-in sensor and to verify its result, the tip of the linear position sensor (LVDT sensor) is attached to the sheet metal to provide the reference data.

A comparison result among the analytics, electromagnetic simulations, and lab-scale experiments of AA3003 sheet having 0.76 mm thickness is graphically presented in Fig. 12. Note that the transducers have inner loops and nonlinear end effects, which reduce the working linear range down to approximately 60 mm, as seen in the experimental result. The induced voltages obtained from the experiment show lower values than those of the electromagnetic simulation and analytical model. This is due to the fact that the gap between the two transducers slightly increases during sheet sliding, which is difficult to control precisely in the experiment. The analytical model provides lower induced voltages than those of the electromagnetic simulation because the electromagnetic properties of sheet material are not considered in the analytical model. Although the results obtained from these three methods show different induced voltage values, all of them provide good linearity between induced voltage and sheet displacement.

In order to observe the linearity between the induced voltage and sheet displacement of these three methods among various

sheet thickness values, the slope (induced voltage over sheet displacement) is calculated and compared as shown in Fig. 13. The shift in the slope between those of the experiment and those of the analytical or simulation results is due to the fact that the gaps in the experiments were not exactly the same as those of the analytics and simulations. In the experiments, while the sheets were initially set to be closely in touch with the sensing area as specified, it was observed that gaps occurred between them and the draw-in sensors during their movement, leading to lower induced voltages. To address this issue, the slopes were plotted against the measured thickness of the sheets, in order to observe if the measurement results were consistent over different gaps between the sheets and the sensors. As shown in Fig. 13, the slopes of all the three configurations provide the same trends over the increased sheet thickness (i.e., gap heights). This confirms that one can use the analytical model and electromagnetic simulation to anticipate the expected slope once a new design or a new material is in place.

3 Experimental Setup and Sensor Measurements

The draw-in and pressure sensors have been integrated into the binders and punch of a large-scale experimental setup [23]. The present work incorporates the findings of Ref. [23] with data from draw-in sensors to create PDI maps, which demonstrate the interplay between the die/binder pressure distribution and sheet material movement, thus presenting a clearer overview of the stamping process, at the system's level. The stamping experiment forms a 432 mm × 508 mm aluminum panel from a 1.56 mm AA5182 blank on a 150 ton double action HPM hydraulic press. The tool

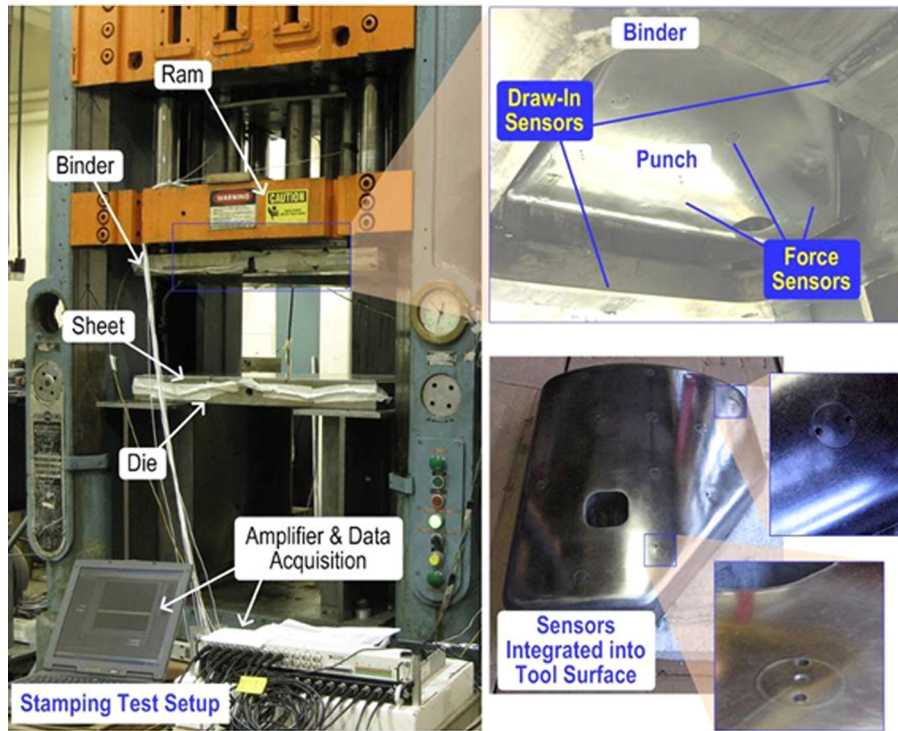


Fig. 14 Large-scale experimental setup with tooling-integrated force and draw-in sensors

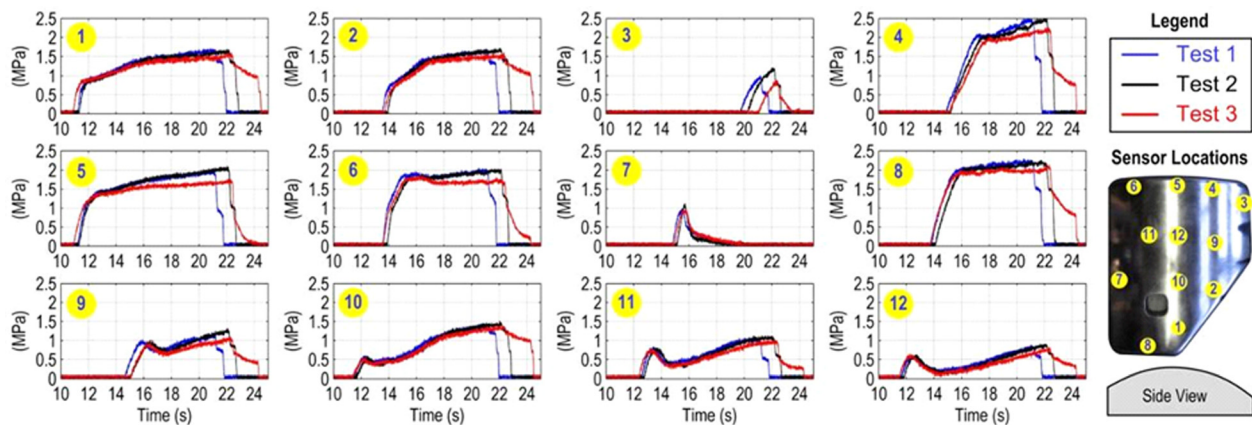


Fig. 15 Pressure measured at 12 locations in three repeated tests [10]

setup consists of the punch, the die, and the binder. A total of 12 dynamic force sensors are integrated into the punch structure using the top-mount sensor integration technique. Five mutual inductance based draw-in sensors were integrated into the binder. The binder force is applied by four corner mounted hydraulic actuators and is measured by load cells. The experimental setup and the sensors are illustrated in Fig. 14. This section presents the measurements from the tooling-integrated sensors and discusses their significance.

3.1 Pressure Measurements. The force sensor measurements from the sensors embedded in the punch are used to estimate the contact pressure at the sensor site. Pressure at the sensor locations is determined by dividing the sensor output by the area of the sensing element (2.85 cm^2). The experiments are performed for five binder (edge clamping) forces and draw depths, with each test repeated three times. Figure 15 shows the scaled pressure measurements for an experiment with 100 mm

draw depth and 400 kN binder force, where good repeatability is observed. It can be seen that different locations on the punch exhibit distinct pressure signatures. For instance, sensors 1, 5, 10, and 12 are the first to sense the pressure increase, due to their position on the crest of the punch curvature. Of these four locations, 1 and 5 recorded larger pressures as they are close to the edges. Sensors 9, 10, 11, and 12 experienced much less pressure due to their internal locations on the punch face. The initial dip in the measured pressure can be attributed to the sliding of the sheet metal on the punch face. The late peak observed in most of the sensor measurements occurs when the punch is close to the bottom of the stroke. At this time, the rounded corners and edges are being formed, creating the high pressure. Sensors 7 and 3, being farthest away from the punch crest, are the last to come into contact and experience little pressure. This effect is more pronounced at location 3 as it sits lower on the punch face.

The difference in the sensor locations is further reflected in the distinctly different pressure signatures they have been associated

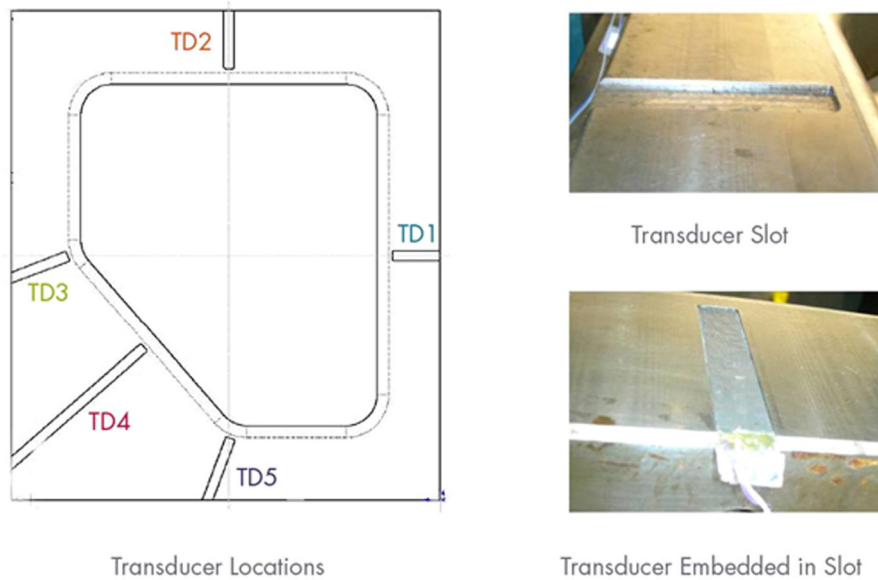


Fig. 16 TD locations in the die and binder

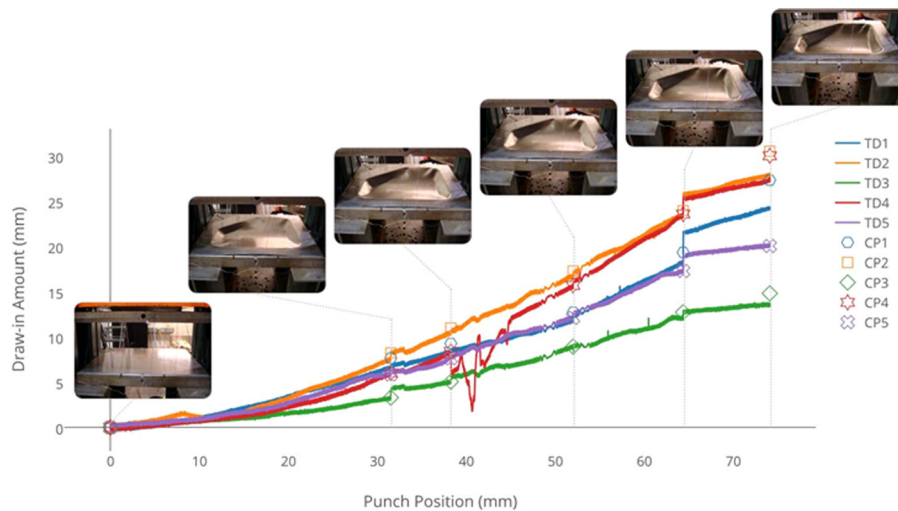


Fig. 17 Draw-in amount versus punch position of the stamping test of AA5182 having 1.56 mm thickness

with. In Sec. 4, these spatially discrete sensor measurements are used to estimate a spatially continuous estimate of the pressure distribution.

3.2 Draw-In Measurements. In order to determine its feasibility and functionality, the draw-in sensors are later installed in a $1\text{ m} \times 1\text{ m}$ die and binder as shown in Fig. 16 and tested in the hydraulic press (Fig. 14). In Fig. 16, “TD” represents “draw-in transducer” and each transducer has a prescribed number for all the five locations. The die and binder of a door-shape are machined to create slots for embedding the transducers as displayed on the right of Fig. 16.

In each stamping test, the tested sheet (AA5182 having 1.56 mm thickness) is placed in between the die and binder, and the punch is set to move down, deforming the sheet, at different drawing positions. During the entire stamping test, the transducers detect the movement of the sheet and provide the changing induced voltages. The punch position is recorded by a displacement sensor mounted on the hydraulic press and later mapped with the draw-in amounts obtained from the draw-in sensor to

obtain continuous real-time draw-in histories at those five locations. The draw-in amounts reported from the developed sensors in this stamping process are compared with those obtained from using a caliper to measure the draw-in amounts at those five locations after each stamping step. The drawback of using caliper was its inability to capture the entire draw-in histories; only discrete draw-in amounts are obtained from the manual measurements. The results from the draw-in sensor (denoted as TD) and manual measurements using a caliper are shown in Fig. 17. Note that only one test sheet is used for all the stamping steps. At the end of each step, sheet metal would springback and therefore, resulted in the discontinuity observed from the draw-in sensors. The plot presents the combined draw-in sensor results of all the stamping steps versus the punch position. As can be seen in Fig. 17, the two methods provide similar results at all five draw-in locations while the draw-in sensors provide the continuous draw-in histories.

4 Reconstruction of Pressure Distribution

The estimation of a continuous pressure distribution on the tool-workpiece interface from measurements made by an array of

discretely positioned sensors is a challenging problem. In this section, the issue of estimation has been approached as a regularization problem. It is solved through the thin-plate splines energy minimization technique, a special case of regularization. A Bayesian technique to leverage a priori knowledge of the pressure distribution by integrating it into the calculation of the pressure estimation is also examined in this section. Specifically, the Bayesian framework is utilized to integrate prior knowledge of the pressure distribution available in the form of an FEA simulated results with sensor measurements to improve the spatial resolution of pressure estimation.

4.1 Numeric Technique: Regularization and Thin Plates Splines. The problem of determining the actual contact pressure distribution P from the set of the sensor measurements v is insufficiently constrained to achieve a unique solution. That is, there exist multiple pressure field solutions that can satisfy all the sensor measurements. The selection of one solution from the multitude of possible solutions can be achieved by regularization. Regularization is a mathematical approach for solving ill-posed problems through assumed restrictions on the smoothness of the final pressure solution [24]. The regularization-based approach to the current problem is to find a surface P^* that minimizes a total energy criteria $E_T(P)$ defined below [25]. The particular surface P^* that minimizes $E_T(P)$ is referred to as the regularized solution

$$E_T(P) = (1 - \lambda)\varepsilon_d(P, v) + \lambda\varepsilon_p(P) \quad (5)$$

Here, $\varepsilon_d(P, v)$ is the component of the total energy function that measures the accuracy of the fit between the regularized solution and the measured data v . The smoothness constraint discussed before is embodied in the second energy term $\varepsilon_p(P)$, also called the stabilizing function. The symbol λ indicates the regularization parameter that controls the balance between having a regularized surface P^* that perfectly satisfies all the input measurements v at the risk of having a noisy solution versus a P^* that may not satisfy all the input data perfectly but has continuity and smoothness characteristic of most natural phenomena.

The accuracy measure that quantifies the goodness-of-fit between a pressure solution $P(x, y)$ and the measured data v_i is written as

$$\varepsilon_d(P, v) = \frac{1}{2} \sum_{i=1}^n \sigma_i^{-2} (P(x_i, y_i) - v_i)^2 \quad (6)$$

Here, n is the number of data points or sensors, and the i th sensor located at coordinates (x_i, y_i) has a measurement variance of σ_i^2 . The stabilizing energy function $\varepsilon_p(P)$ can have many forms with the only criteria being that lower energy leads to a more smoother surface. Commonly used forms of smoothness functions are based on physical principles, such as energy of a membrane (Eq. (7)), under the assumption of small in-plane deformations and the energy of a surface (Eq. (8)), under small out-of-plane deformations [24]

$$\varepsilon_p^{\text{Membrane}}(P) = \frac{1}{2} \iint \left(\left(\frac{\partial P}{\partial x} \right)^2 + \left(\frac{\partial P}{\partial y} \right)^2 \right) dx dy \quad (7)$$

$$\varepsilon_p^{\text{Surface}}(P) = \frac{1}{2} \iint \left(\left(\frac{\partial^2 P}{\partial x^2} \right)^2 + 2 \left(\frac{\partial^2 P}{\partial xy} \right)^2 + \left(\frac{\partial^2 P}{\partial y^2} \right)^2 \right) dx dy \quad (8)$$

Equation (8) is the same as the minimization objective for thin plate spline (TPS)-based surface interpolations [26]; thus, TPS interpolation is recognized as a special case of regularization, where putting the regularization parameter $\lambda = 1$ in Eq. (2) gives

$$E_T(P) = \varepsilon_p(P) \quad (9)$$

A numerical approach that uses radial basis functions to find the pressure field that minimizes Eq. (9) has been presented in prior work [26]. In Sec. 4.2, a Bayesian framework for integrating prior knowledge of the pressure distribution available in the form of an FEA simulated results with experimental sensor measurements is presented.

4.2 Model-Based Technique: Bayesian Inference. In certain scenarios, it is possible that a pre-existing model of the pressure distribution at the punch-workpiece interface is available. The pre-existing model could be in the form of FE simulations of the stamping process. Thus, it is desirable to have a mathematical framework for combining information from a pre-existing model with the new current information coming from sensor measurements. This work expands on a recently proposed engineering-statistical modeling approach that uses the Bayes method to update the engineering model through the sensor measurements based statistical model [27]. Specifically, the existing mathematical framework has been adjusted to accommodate two independent spatial variables to describe the time-varying data fields.

It is noted that the engineering model needs to mimic the physical system sufficiently well, this may be quantified by defining a model adequacy index of the form proposed in Ref. [27]. Given that this preliminary condition is met, the pressure field results from the FEA model can be extracted as a set of nodal reading of the form

$$P_{\text{FEA}}(x, y, t) = f(x, y, x_i^n, y_i^n, p_i^{\text{FEA}}(t)) \quad i \in 1..N \quad (10)$$

Here, N is the number of nodes in the FE mesh of the contact surface. (x_i^n, y_i^n) is the location of the i th FE mesh node, and $p_i^{\text{FEA}}(t)$ is the FE simulated pressure at node i at time instant t . $P_{\text{FEA}}(x, y, t)$ is the pressure at time instant t at any location (x, y) which does not necessarily coincide with a node location and f can be any linear or subdivision based interpolation function [28]. Since FE mesh tends to be dense, the estimation errors introduced due to f are small and can be ignored. $P_{\text{FEA}}(x, y, t)$ is used to calculate $f_i(t)$ which is the FE estimated pressure at the location of the i th sensor, which is (x_i^s, y_i^s)

$$f_i(t) = P_{\text{FEA}}(x_i^s, y_i^s, t) \quad i \in 1..S \quad (11)$$

Here, S is the total number of sensors used in the experiment. In the analysis that follows, $f_i(t)$ represents the prior knowledge about the pressure distribution. The experimental measurements from the sensors are represented as

$$y_i(t) = P_{\text{EXP}}(x_i^s, y_i^s, t) \quad i \in 1..S \quad (12)$$

Here, $P_{\text{EXP}}(x_i^s, y_i^s, t)$ is the pressure measured at time instant t by the i th sensor located at (x_i^s, y_i^s) . When the experiment is repeated n times, the additional measurements are included in $y_i(t)$ such that its length becomes $n \times S$, and $f_i(t)$ is padded with repeated values to match its length. In the analysis that follows, $y_i(t)$ represents the new knowledge about the pressure distribution. Having laid out the datasets and ignoring random errors, the constant adjustment model based on the model proposed in Ref. [29] is given as

$$P(t) = f(t) + \beta_0(t) + \beta_1(t)(f(t) - \bar{f}(t)) \quad (13)$$

Here, $P(t)$ is the constant adjustment model. β_0 and β_1 are the additive and multiplicative bias for the estimated pressure modeled as zero mean normal distributions with a variance of τ_0^2 and τ_1^2 , respectively. $\bar{f}(t)$ is the mean FE calculated pressure across the sensor locations at time t . Following the method, matrices \mathbf{F} and $\mathbf{\Sigma}$ are defined as

$$\beta(t) = \begin{bmatrix} \beta_0(t) \\ \beta_1(t) \end{bmatrix} F(t) = \begin{bmatrix} 1 & f_1(t) - \bar{f}(t) \\ 1 & f_2(t) - \bar{f}(t) \\ \vdots & \vdots \\ 1 & f_{ns}(t) - \bar{f}(t) \end{bmatrix} \Sigma = \begin{bmatrix} \tau_0^2 & 0 \\ 0 & \tau_1^2 \end{bmatrix} \quad (14)$$

Whereupon, the posterior distribution of $\beta(t)$ can be expressed as [30]

$$\beta|P_{\text{EXP}}(x, y, t) \sim \mathbb{N}((F'F + \sigma^2(t)\Sigma^{-1})^{-1}F'(F\beta(t)), \sigma^2(t)(F'F + \sigma^2(t)\Sigma^{-1})^{-1}) \quad (15)$$

Here, $\sigma^2(t)$ is the variance of the sensor measurements at time instant t when the experiment is repeated n times. If the posteriors of the additive and multiplicative bias are denoted as $\hat{\beta}_0$ and $\hat{\beta}_1$, respectively, the constant adjustment pressure predictor $P_{\text{CAM}}(x_k, y_k, t)$ calculated over a computation grid of M points (x_k, y_k) will look like

$$P_{\text{CAM}}(x_k, y_k, t) = P_{\text{FEA}}(x_k, y_k, t) + \hat{\beta}_0(t) + \hat{\beta}_1(t) \times (P_{\text{FEA}}(x_k, y_k, t) - \bar{f}(t)) \quad k \in 1..M \quad (16)$$

Optimized posterior bias $\hat{\beta}_0(t)$ and $\hat{\beta}_1(t)$ are calculated by maximum likelihood estimation [27]

$$\hat{\beta}_0(t) = \left(1 - \frac{1}{z_0^2(t)}\right)_+ \tilde{\beta}_0(t) \quad \hat{\beta}_1(t) = \left(1 - \frac{1}{z_1^2(t)}\right)_+ \tilde{\beta}_1(t) \quad (17)$$

where in z_0 and z_1 take the values

$$z_0(t) = \frac{\sqrt{n}|\tilde{\beta}_0(t)|}{\sigma(t)} \quad z_1(t) = \frac{\sqrt{Q(t)}|\tilde{\beta}_1(t)|}{\sigma(t)} \quad (18)$$

$$Q(t) = \sum_{i=1}^{ns} (f_i(t) - \bar{f}(t))^2$$

Here, $\tilde{\beta}_0(t)$ and $\tilde{\beta}_1(t)$ are least square estimates of $\beta_0(t)$ and $\beta_1(t)$ and are calculated as

$$\tilde{\beta}_0(t) = \bar{y}(t) - \bar{f}(t) \quad \tilde{\beta}_1(t) = \sum_{i=1}^{ns} (y_i(t) - f_i(t))(f_i(t) - \bar{f}(t))/Q(t) \quad (19)$$

Equation (19) is central to combining the prior model represented by the FEA results with the new information provided by the sensor measurements. The results of this technique are discussed in Sec. 5.

5 Results and Discussion

The thin-plate spline technique presented in Sec. 4.1 and the Bayesian model based reconstruction technique discussed in Sec. 4.2 have been evaluated using the experimental data collected on the full-scale stamping experiment illustrated in Fig. 14. An FEA model of the process presented in previous work [31] has been used as the prior model for the Bayesian analysis. The present paper builds on the previous work by combining information from experiments and FEA in a stochastic framework, extending the spatially weighted blending function as described in Ref. [31]. This presents an improvement in estimating the pressure distribution in areas where sensor coverage is sparse, whereas FEA models exist for filling in information in the spatial regions of low sensor density. Specifically in the pressure experiments described in Sec. 3.1 of this paper, the sensor density is sufficiently high,

and the geometric features on the die are smooth and sharp changes in pressure are not expected. Therefore, a reconstruction based purely on sensor data through TPS is effective. The stochastic method presented in Sec. 4.2 provides a good alternative for scenarios where this is not the case.

5.1 Pressure Reconstruction. Figure 18 illustrates the pressure distribution on the punch–workpiece interface at different time instants during the stamping process. The left most column shows the pressure distribution as estimated by FE simulations of the process. The right most column displays the pressure distribution estimated from the sensor measurements using thin-plate splines interpolation. The FE simulation results by virtue of the fine computation grid used have a high spatial resolution and indicate the presence of small features in the pressure distribution such as that present at the center of the die at $T = 12$ s. It is noted that FE simulation results though rich in resolution and spatial features do not account for process variations that may crop up during an actual stamping process. The TPS results given on the right most column are based on the measurements of the 12 top-mount sensors illustrated in Fig. 15. Due to the sparse coverage of the tool surface by the embedded sensors, TPS results are less well defined and have a lower spatial resolution compared to FE results. The redeeming feature of the TPS-based pressure estimations is that they are sensitive to the variations that take place in the stamping process. The center column shows the results of the model-based reconstruction technique discussed in Sec. 4.2.

The contact pressure graphs indicate that all the three methods successfully identify the initial point of contact between the punch and the sheet metal. As the process progresses, the initial point of contact which is at the center of the punch due to its curved shape spreads out along the punch corners. It is noted that the FE simulation model overpredicts the pressure distribution as compared to the sensor measurements, the Bayesian model in the center combines the two information sources to achieve an estimate that realistically depicts the magnitude of the pressure while retaining the spatial features of the simulated results.

5.2 Stamping PDI Map. The information from the embedded punch sensors, the draw-in sensors embedded on the die flange, and sensors mounted on the binder hydraulic actuators has been combined and presented in a single stamping PDI map in Fig. 19. The thin-plate spline interpolation technique has been used to interpolate the pressure on the binder and the punch. The draw-in measurements are represented by vectors placed as the draw-in sensor locations. For visual clarity, the vector length is three times the actual draw-in amount. The vector direction is aligned along the sensing axis of the draw-in sensor. The sketch inset on the top left of the figure illustrates the positions of the various sensors on the stamping tools.

It is of interest to note the correlation between the material flow and the pressure distribution. In the initial few seconds into the process, the binder pressure at the top right corner is lowest, in this period the punch comes into contact with the sheet metal. The geometry of the punch causes the initial contact area to be spread out along the center of the punch. As the punch moves further into the sheet metal, the area of initial contact increases as well as the magnitude of pressure becomes higher. It is observed that the contact pressure increases along the punch edges this is because of the initial forming of the corners on the sheet metal part. The forward motion of the punch causes more sheet metal material to flow into the die and it does so along the path of least resistance. Since the sheet metal is restrained on all the sides, the material motion initiates in the region of least pressure. In this case the top right corner. This is most noticeable at time $T = 2$ s, where the two top right draw-in sensors indicate a material motion of 10 mm and 7 mm while the rest indicate negligible movement. As the process progresses, the continuing motion of the punch is opposed by the binder force and results in increasing contact pressure on the

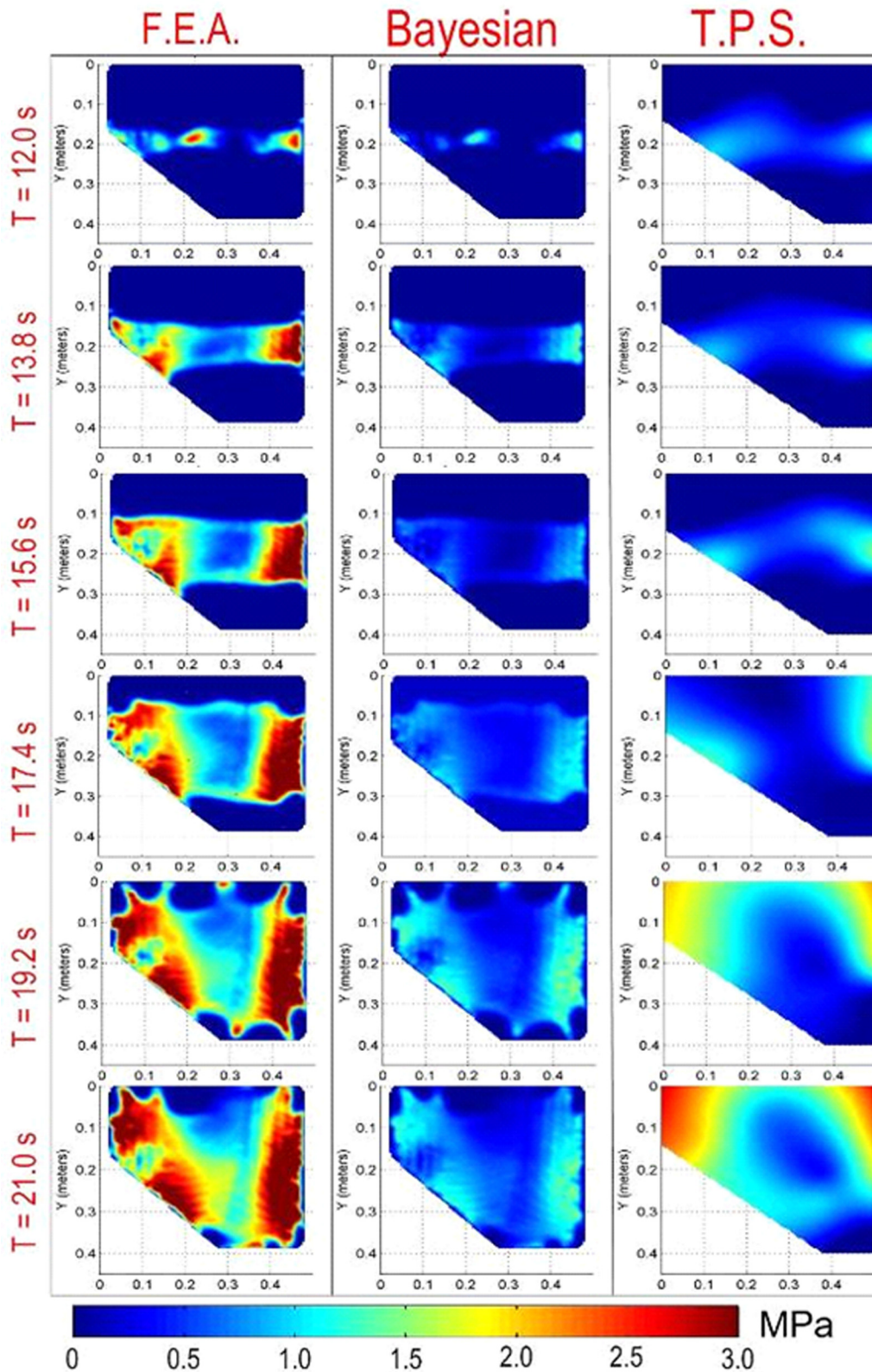


Fig. 18 Contact pressure at punch-workpiece interface estimated by FEA, Bayesian, and TPS

punch surface. This leads to further increases in material draw-in from all the sides. It is noted that the regions with least binder pressure keep a lead on the material draw-in. Another interesting observation is that compared to the binder pressure distribution, the punch pressure distribution shows a lot more transient pressure features which are indicative of the process dynamics. The impact

of these features on the part quality is topic of continuing research.

In order to establish a correlation between the tool-workpiece pressure distribution and the material draw-in, a second experiment was performed. In this second experiment, the binder actuator controller was tweaked to provide a more uniform binder pressure

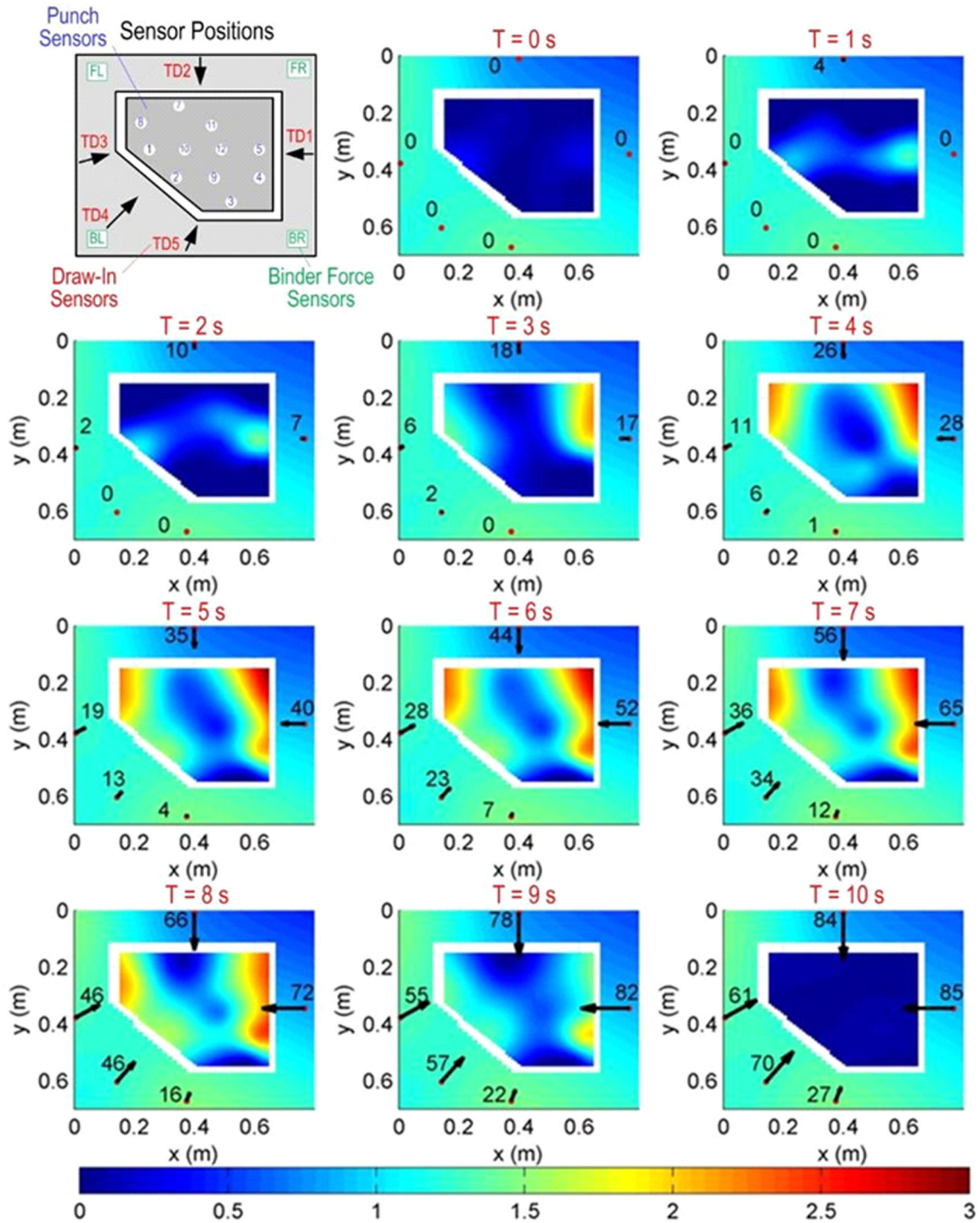


Fig. 19 PDI map of the stamping process indicating pressure distribution (MPa) and draw-in ($3 \times \text{mm}$)

distribution. The PDI maps for this experiment are illustrated in Fig. 20. The effect of this minor adjustment is that the binder pressure distribution is more uniform. During the process, the material draw-in now begins at the lower left corner which has a relatively smaller binder pressure. On comparing PDI maps for the two experiments, it is interesting to note that the uniformity of the binder pressure distribution leads to a more balanced punch pressure distribution and to large changes in the final draw-in amounts. This is best seen by comparing the PDI maps at $T = 9 \text{ s}$. The PDI maps and the related tooling-integrated PDI sensing technology

allow a new level of observability in the stamping process. These results can be used to quantify process variations in sheet metal stamping and further used for process control to reduce product disparities. Additionally, new products and processes can be designed based on the quantified and referenced variations.

6 Conclusions

This paper describes two complementary tooling-integrated sensing methods that collectively enables comprehensive and

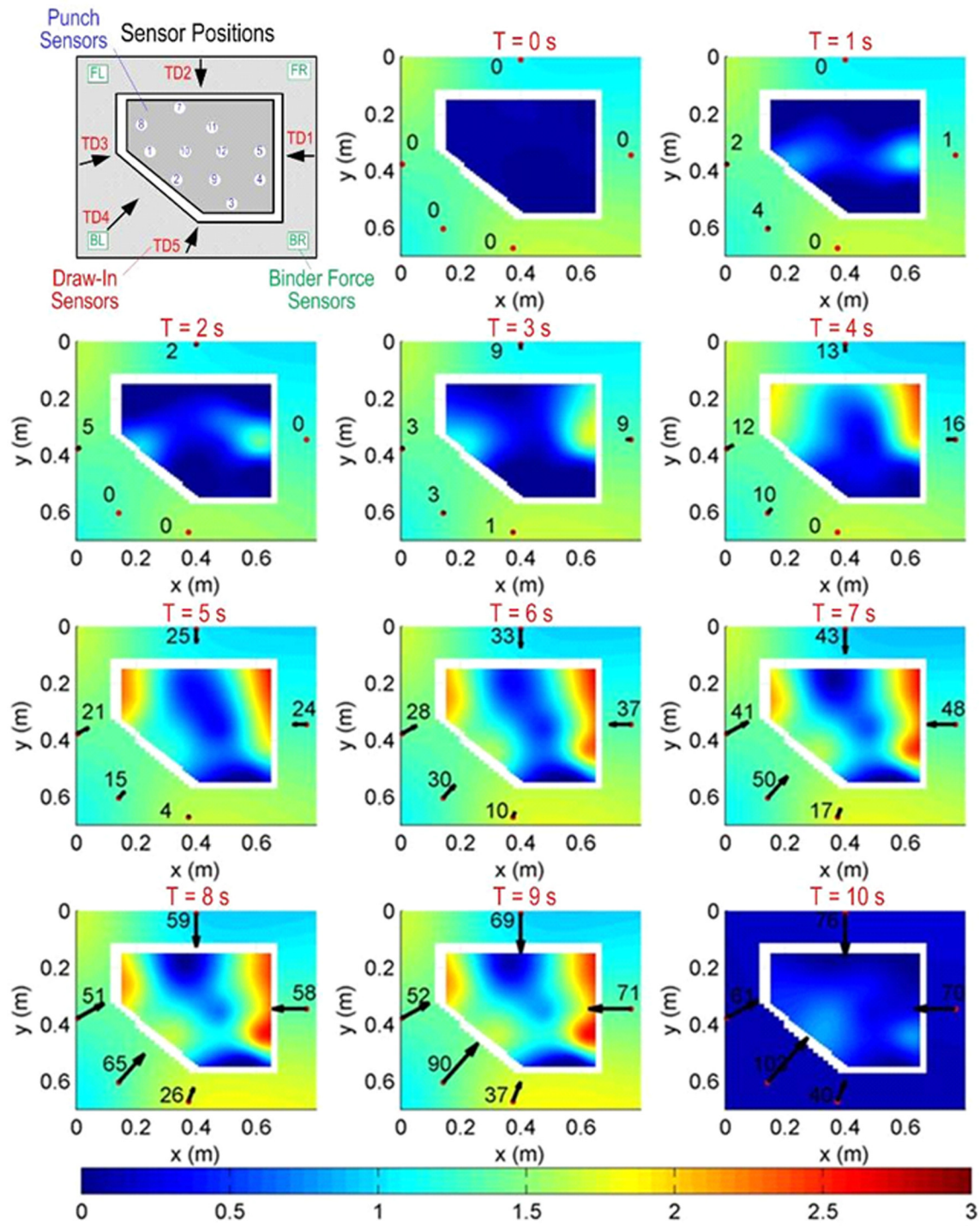


Fig. 20 PDI map of the stamping process indicating pressure distribution (MPa) and draw-in ($3 \times \text{mm}$)

simultaneous monitoring of the dynamics and kinematics of the sheet metal stamping process, thus more clearly reveals the physics underlying the process than previous techniques. The analytical bases for the sensing methods are introduced, and the performance was experimentally evaluated. Specifically, the non-contact draw-in sensors embedded in the binders were found to respond linearly to the sheet displacement, thereby simplifying data capturing and processing. For pressure sensing, a top-mount method is developed, and numerical and model-based techniques for reconstructing the pressure distribution at the tool-workpiece interface from the spatially distributed sensors are experimentally

evaluated. Both the thin-plate splines method and the Bayesian inference method were investigated for pressure data evaluation, depending on the availability of prior knowledge about pressure distribution. Analysis of the results, facilitated by the developed PDI maps that combine spatiotemporal information into an illustrative representation, reveals a strong correlation between the pressure distribution at the tool-workpiece interface and material draw-in. Measurements performed on a real-world stamping machine indicate that the tooling-integrated sensing techniques can contribute to improving the modeling, diagnosis, and optimization of the sheet metal stamping process to achieve better part

quality control, thus advancing the state-of-the-knowledge of this important manufacturing process.

Acknowledgment

The authors greatly appreciate the funding provided to this research by the National Science Foundation under CMMI-0620972/0620957.

References

- [1] Hasan, R., Kasikci, T., Tsukrov, I., and Kinsey, B. L., 2013, "Numerical and Experimental Investigations of Key Assumptions in Analytical Failure Models for Sheet Metal Forming," *ASME J. Manuf. Sci. Eng.*, **136**(1), p. 011013.
- [2] Ahmetoglu, M. A., Altan, T., and Kinzel, G. L., 1992, "Improvement of Part Quality in Stamping by Controlling Blank-Holder Force and Pressure," *J. Mater. Process. Technol.*, **33**(1), pp. 195–214.
- [3] Hsu, C. W., Ulsoy, A. G., and Demeri, M. Y., 2002, "Development of Process Control in Sheet Metal Forming," *J. Mater. Process. Technol.*, **127**(3), pp. 361–368.
- [4] Lin, Z. Q., Wang, W. R., and Chen, G. L., 2007, "A New Strategy to Optimize Variable Blank Holder Force Towards Improving the Forming Limits of Aluminum Sheet Metal Forming," *J. Mater. Process. Technol.*, **183**(2–3), pp. 339–346.
- [5] Cao, J., and Boyce, M. C., 1997, "A Predictive Tool for Delaying Wrinkling and Tearing Failures in Sheet Metal Forming," *ASME J. Eng. Mater. Technol.*, **119**(4), pp. 354–365.
- [6] Ahmetoglu, M. A., Broek, T. R., Kinzel, G., and Altan, T., 1995, "Control of Blank Holder Force to Eliminate Wrinkling and Fracture in Deep-Drawing Rectangular Parts," *CIRP Ann. Manuf. Technol.*, **44**(1), pp. 247–250.
- [7] Ge, M., Du, R., Zhang, G., and Xu, Y., 2004, "Fault Diagnosis Using Support Vector Machine With an Application in Sheet Metal Stamping Operations," *Mech. Syst. Signal Process.*, **18**(1), pp. 143–159.
- [8] Majeske, K. D., and Hammett, P. C., 2003, "Identifying Sources of Variation in Sheet Metal Stamping," *Int. J. Flexible Manuf. Syst.*, **15**(1), pp. 5–18.
- [9] Doolan, M. C., Kalyanasundaram, S., Hodgson, P., and Hall, M. C., 2001, "Identifying Variation in Sheet Metal Stamping," *J. Mater. Process. Technol.*, **115**(1), pp. 142–146.
- [10] Souza, T. D., and Rolfe, B., 2008, "Multivariate Modelling of Variability in Sheet Metal Forming," *J. Mater. Process. Technol.*, **203**(3), pp. 1–12.
- [11] Garcia, D., Orteu, J. J., and Penazzi, L., 2002, "A Combined Temporal Tracking and Stereo-Correlation Technique for Accurate Measurement of 3D Displacements: Application to Sheet Metal Forming," *J. Mater. Process. Technol.*, **125–126**, pp. 736–742.
- [12] Lim, Y., Venugopal, R., and Ulsoy, A. G., 2014, *Process Control for Sheet Metal Stamping*, Springer, London.
- [13] Nelson, A. W., Malik, A. S., Wendel, J. C., and Zipf, M. E., 2014, "Probabilistic Force Prediction in Cold Sheet Rolling by Bayesian Inference," *ASME J. Manuf. Sci. Eng.*, **136**(4), p. 041006.
- [14] Kernosky, S. K., Weinmann, K. J., Michler, J. R., and Kashani, A. R., 1998, "Development of a Die Shoulderforce Transducer for Sheet Metal Forming Research," *ASME J. Manuf. Sci. Eng.*, **120**(1), pp. 42–48.
- [15] Du, H., and Klamecki, B. E., 1999, "Force Sensors Embedded in Surfaces for Manufacturing and Other Tribological Process Monitoring," *ASME J. Manuf. Sci. Eng.*, **121**(4), pp. 739–748.
- [16] Lo, S. W., and Yang, T. C., 2004, "Closed-Loop Control of the Blank Holding Force in Sheet Metal Forming With a New Embedded-Type Displacement Sensor," *Int. J. Adv. Manuf. Technol.*, **24**(7–8), pp. 553–559.
- [17] Doege, E., Seidel, H. J., Griesbach, B., and Yun, J. W., 2002, "Contactless On-Line Measurement of Material Flow for Closed Loop Control of Deep Drawing," *J. Mater. Process. Technol.*, **130**, pp. 95–99.
- [18] Sah, S., 2011, "Embedded Sensing and Characterization of Contact Pressure Distributions for Advanced Stamping Process Monitoring," *Ph.D. dissertation*, University of Connecticut, Storrs, Toronto, CT.
- [19] Halliday, D., Resnick, R., and Walker, J., 1997, *Fundamentals of Physics Extended*, Wiley, Canada, pp. 729–732.
- [20] Kopczyński, P., 1992, "LVDTs, Theory and Application," *Sensors*, **9**, pp. 18–22.
- [21] Cao, J., Lee, J. H., and Peshkin, M., 2004, "Real-Time Draw-In Sensors and Methods of Fabrication," *U.S. Patent No. 6,769,280*.
- [22] Saslow, W. M., 2002, "How Electric Currents Make Magnetic Field: The Biot-Savart Law and Ampère's Law," *Electricity, Magnetism, and Light*, Academic Press, Cambridge, MA, pp. 460–504.
- [23] Gao, R., Sah, S., and Mahayotsanun, N., 2010, "On-Line Measurement of CPD at Tool-Workpiece Interfaces in Manufacturing Operations," *Ann. CIRP*, **59**(1), pp. 399–402.
- [24] Tikhonov, A. N., and Arsenin, V. Y., 1977, *Solutions of Ill-Posed Problems*, Winston, New York.
- [25] Szeliski, R., 1990, "Bayesian Modeling of Uncertainty in Low-Level Vision," *Int. J. Comput. Vision*, **5**(3), pp. 271–301.
- [26] Terzopoulos, D., 1986, "Regularization of Inverse Visual Problems Involving Discontinuities," *IEEE Trans. Pattern Anal. Mach. Intell.*, **8**, pp. 413–424.
- [27] Roshan Joseph, V., and Melkote, S. N., 2009, "Statistical Adjustments to Engineering Models," *J. Qual. Technol.*, **41**, pp. 362–375.
- [28] Dyn, N., Levine, D., and Gregory, J. A., 1990, "A Butterfly Subdivision Scheme for Surface Interpolation With Tension Control," *ACM Trans. Graphics*, **9**(2), pp. 160–169.
- [29] Fuentes, M., and Raftery, A., 2005, "Model Evaluation and Spatial Interpolation by Bayesian Combination of Observations With Outputs From Numerical Models," *Biometrics*, **61**(1), pp. 36–45.
- [30] Bookstein, F. L., 1989, "Principal Warps: Thin Plate Splines and the Decomposition of Deformations," *IEEE Trans. Pattern Anal. Mach. Intell.*, **11**(6), pp. 567–585.
- [31] Sah, S., Gao, R., and Kurp, T., 2011, "Model-Augmented Methods for Estimation of Pressure Distribution," *J. Manuf. Syst.*, **30**(4), pp. 223–233.